Surface Review and Letters, Vol. 9, No. 1 (2002) 223–232

XPEEM WITH ENERGY-FILTERING: ADVANTAGES AND FIRST RESULTS FROM THE SMART PROJECT

TH. SCHMIDT,* U. GROH, R. FINK and E. UMBACH†
Experimentelle Physik II, Universität Würzburg, Am Hubland, D-97074 Würzburg, Germany
* *Thomas.Schmidt@physik.uni-wuerzburg.de*

O. SCHAFF, W. ENGEL, B. RICHTER, H. KUHLENBECK, R. SCHLÖGL, H.-J. FREUND and A. M. BRADSHAW
Fritz-Haber-Institut der Max-Planck-Gesellschaft, Faradayweg 6-8, D-14195 Berlin, Germany

D. PREIKSZAS, P. HARTEL, R. SPEHR and H. ROSE
Angewandte Physik, Hochstuhlstraße 6, D-64289 Darmstadt, Germany

G. LILIENKAMP and E. BAUER‡
Physikalisches Institut, Technische Universität Clausthal, Leibnizstraße 4, D-38678, Germany

G. BENNER
LEO Elektronenmikroskopie GmbH, D-73446 Oberkochen, Germany

The second development step of the SMART project, i.e. an energy-filtered but not yet corrected photoelectron emission microscope, operates at the undulator U49/1-PGM beamline at BESSY II. It already demonstrates the variety of methods of the final version: microscopy, spectroscopy and electron diffraction. Some recent experimental results are reported for these three operation modes. In addition, the theoretical improvement of lateral resolution and transmission of PEEMs in general by using an energy filter is discussed for systems without and with aberration correction.

1. Introduction

The ongoing miniaturization in technological devices and the progress in surface science demand novel instrumental methods for surface characterization on a length scale of only a few atomic distances. Up to now, the state-of-the-art instruments for that purpose are scanning electron microscopes (SEM), with a resolution limit of several nanometers, atomic force (AFM) and scanning tunneling microscopes (STM). The latter can investigate the film morphology and geometric structure of surfaces on an atomic scale. However, the disadvantages, especially of scanning probe microscopes, are (a) the relatively slow data acquisition due to serial detection, (b) the restriction to the topmost surface layer, and especially (c) the fact that they do not allow a sufficient spectroscopic,

*Corresponding author.
†Project coordinator.
‡Permanent address: Department of Physics and Astronomy, Arizona State University, Tempe, AZ 85287-1504, USA.

i.e. electronic and chemical, analysis. Alternative techniques are the direct imaging PEEM (photoelectron emission microscope) or — slightly more sophisticated — the LEEM (low-energy electron microscope) combined with an imaging analyzer and a tunable high-brilliance synchrotron radiation source. Besides the fast imaging (a few tens of milliseconds time scale due to parallel detection) which allows the *in situ* and real time study of processes like growth,[1,2] surface reaction,[3] annealing, phase transitions, etc., these spectromicroscopes enable a comprehensive spectroscopic analysis on a length scale corresponding to their lateral resolution.[4] The lateral resolution limit has been reduced in the last few decades, but is limited to 5 nm in LEEM[5] and to about 10–20 nm in spectroscopic PEEM[6,7] by the unavoidable spherical and chromatic aberrations of rotationally symmetric lenses.[8] The SMART project[9] will overcome this limit by introducing an electrostatic mirror[10] together with a highly symmetric magnetic beam splitter[11] in an optimized optical design. This corrector compensates for the spherical and chromatic aberrations as recently demonstrated[12] and will improve the lateral resolution by a factor of 5–10. Simultaneously, it will increase the transmission by a factor of 25–100. Further on, the instrument is equipped with a special imaging analyzer: the so-called OMEGA filter,[13] which enables energy-filtered imaging and spectroscopy. When the instrument is completed it will achieve a lateral resolution which is hopefully close to the theoretical resolution limit of 0.5 nm at an energy resolution of 100 meV. Hence the presently attainable resolution can be improved by a factor of 5–10. As a result new possibilities in surface science and investigations of nanoscaled technological devices will be opened.

There are other groups in the world, who will apply or even already use energy-filtered PEEMs at third generation synchrotron beamlines, e.g. the commercial Focus PEEM with a retarding field analyzer as an imaging filter developed in Schönhense's group,[14] the commercial ELMITEC spectroscopic PEEM/LEEM ("SPELEEM") with a 180° hemispherical analyzer developed in Bauer's group,[6] which will be installed at ELETTRA (Italy) and at the SLS (Swiss).[15] The PEEM III[16] instrument being developed at the ALS (Berkeley, USA) will be equipped with a corrector system similar to that of the SMART, but is presently planned without an energy filter. Delong Instruments (Brno, Czech Republic) has started to operate an energy-filtering and corrected LEEM/PEEM instrument[17] which will be installed at ELETTRA.

The SMART instrument consists of three main modules that can be tested separately: (1) the measurement chamber with sample manipulator and objective lens, (2) the beam splitter with the correcting mirror and the electron gun, and (3) the transfer optic system with the OMEGA filter and the projection optics. After the first successful tests of the individual modules, the modules (1) and (3) were mounted together, resulting in the current (summer 2001) version of the SMART instrument: a spectroscopic PEEM. In this paper we will report on both the theoretical improvements regarding lateral resolution and transmission with an energy-filtered PEEM without and with a correction system, and on the first experimental results.

2. Experimental Setup

A detailed description of the final instrumental concept of the SMART is given in Ref. 18. Therefore, we restrict ourselves to a brief overview of the surrent experimental setup. The microscope is a UHV instrument with a base pressure of 10^{-10} mbar in the image column, OMEGA filter, and in the measurement chamber. The design of the latter and of the sample manipulator is similar to that developed in Clausthal,[19,20] which enables *in situ* evaporation, heating up to 2300 K and cooling down to 200 K, and gas treatment up to about 10^{-6} mbar even during observation, when the high voltage of 15 kV is applied to the sample.

The sample can be illuminated at grazing incidence of 20° either by the light of a Hg short arc lamp or by synchrotron light. The photoemitted electrons are accelerated into the magnetic objective lens to the base energy of 15 keV. After they pass the five-lens transfer optics with its acceptance-angle-limiting aperture and its area-of-interest-selecting field aperture, the electrons are energy-filtered by the imaging analyzer (OMEGA filter). Finally the projection optics transfers the electrons to the detector. Similar to the lens settings of the SPELEEM,[6] this SMART version allows three modes of operation:

(1) microscopy (i.e. energy filtered imaging, including work function contrast imaging), (2) spectroscopy and (3) imaging of the angular distribution of emitted electrons. Sample preparation can presently be performed in an attached mini-preparation-chamber equipped with sputter unit, sample heating, and sample transfer through an air lock.

The microscope is installed quasipermanently at the U49/1-PGM undulator beamline[21] at BESSY II (Berlin, Germany). The photon energy ranges from 90 eV to 2000 eV with resolving power of $E/\Delta E > 12,000$ at a photon energy of $E = 400$ eV. For an energy resolution of 100 meV at $E = 400$ eV the presently obtainable photon flux of 1×10^{12} ph/s can be focussed into a spot on the sample of 50×20 μm^2 size.

3. Resolution Limit

The SMART instrument employs a magnetic immersion lens which has lower aberration than electrostatic triode or tetrode lenses. This objective lens, together with the corrector and energy filter, determines the resolution limit of the microscope. In the following we discuss the influence of the aberrations for uncorrected systems and subsequently for corrected systems, both equipped with a filter that selects an energy window ΔE for an initial kinetic energy E_0 with which the detected electrons start at the sample surface.

3.1. *Uncorrected systems*

In the case of an uncorrected system we simply define the resolution limit d as

$$d = \sqrt{d_d^2 + (d_s/2)^2 + d_c^2}\,, \tag{1}$$

where d_s and d_c are the radii of the disks of confusion due to spherical and chromatic aberrations of the lens with

$$d_s = C_s \sin^3 \alpha\,, \tag{2}$$

$$d_c = C_c \frac{\Delta E}{E_0} \sin \alpha\,. \tag{3}$$

The diffraction at the aperture yields a spot the radius of which

$$d_d = 0.61\lambda / \sin \alpha \tag{4}$$

increases with decreasing acceptance angle α. (α is the maximum emission angle contributing to the image.) Here $\lambda = \sqrt{1.5/E_0}$ the electron wave length in nm, and E_0 denotes the start energy in eV. The aberration coefficients C_s and C_c depend on the geometry of the lens, on the start energy E_0, and on the base energy E (in our case 15 keV). In the plane of least confusion the radius of the spherical aberration disk is less than half its radius in the Gaussian image plane. As a result the contribution of d_s is reduced by a factor of 2, as given in Eq. (1).

The dependence of the resolution limit d on the acceptance angle α is shown in Fig. 1 for three different start energies E_0 at an energy spread $\Delta E = 0.5$ eV, which is typical for the energy spread in LEEM instruments. The calculations are based on Eqs. (1)–(4) and the aberration coefficients of a magnetic lens suggested by D. Preikszas.[22] However, the general statements are valid for all immersion lenses. The contributions of the chromatic and spherical aberrations and of the diffraction limit are indicated as dashed, dotted and thin solid lines. While the decrease of the acceptance angle lowers the influence of the aberrations, the diffraction behaves just the opposite. As a consequence, there exists an optimum resolution limit at an optimum acceptance angle (thick line). Comparing the behavior for different start energies E_0, the resolution limit decreases with higher start energies: from about 12 nm at $E_0 = 1$ eV to 4 nm at $E_0 = 100$ eV. The reason is that the diffraction limit is lowered

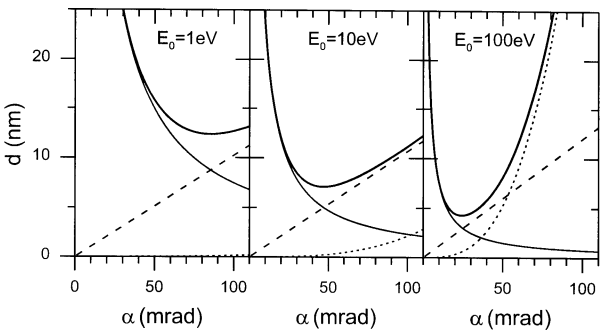

Fig. 1. Resolution limit d of an uncorrected objective lens as a function of the acceptance angle α for different start energies E_0 and a fixed energy spread of $\Delta E = 0.5$ eV (thick, topmost lines). The contributions of the chromatic aberration, spherical aberration and diffraction limit are indicated by the dashed, dotted and thin solid lines.

for higher energies. However, the spherical aberration which is negligibly small compared to the chromatic aberration at low energy, becomes dominant at higher energies.[23] The optimum acceptance angle decreases from 85 mrad to 25 mrad between $E_0 = 1$ eV and $E_0 = 100$ eV. Accordingly, the instrumental transmission $T(\alpha) = 2\sin^2\frac{\alpha}{2} \approx \alpha^2/2$ is reduced by a factor of 10 (assuming isotropic emission). This example shows that the resolution can be improved by a factor of 3, but simultaneously the transmission and hence the image intensity is reduced by a factor of 10.

PEEMs without energy filter use electrons at low start energies between 0 eV and a few eV. The energy spread ΔE is typically in the range of 0.5–1 eV for excitation with a Hg short arc lamp and 2–5 eV with synchrotron light. The spread depends on the photon energy, the excitation condition (e.g. resonant X-ray absorption) and, in the case of a Hg lamp, on the work function. Figure 2 shows the improvement in this working mode (i.e. for $E_0 = 1$ eV) by an energy filter with different energy windows ΔE. Due to the low start energy the chromatic aberration is dominant for $\Delta E = 2$ eV and 0.5 eV. Only for the very small energy window $\Delta E = 0.1$ eV does the spherical aberration become important. For $\Delta E = 2$ eV the optimum resolution limit is about $d = 24$ nm at $\alpha = 44$ mrad. Keeping this resolution, the acceptance angle α can be increased to 240 mrad ($\Delta E = 0.5$ eV) and 540 mrad ($\Delta E = 0.1$ eV). Although the energy-selecting analyzer slit must be narrowed for the latter cases, the image intensity is increased by a factor of 7.5 ($\Delta E = 0.5$ eV) and 7.3 ($\Delta E = 0.1$ eV) because the transmission is improved by a factor of 30 ($\Delta E = 0.5$ eV) and 147 ($\Delta E = 0.1$ eV), respectively, due to the larger acceptance angle. Alternatively, the analyzer reduces the resolution limit from $d = 24$ nm ($\Delta E = 2$ eV) to 12.4 nm ($\Delta E = 0.5$ eV) and 5.6 nm ($\Delta E = 0.1$ eV), whereas the increase in transmission nearly compensates for the loss of image intensity caused by the narrower energy slit.

As a result, the energy filter increases transmission and resolution at low energies, where the chromatic aberration dominates. The gain in image intensity is due to the relation $d_c \propto \Delta E \times \alpha$ for the chromatic aberration [Eq. (3)]. A decrease of ΔE by a factor of g allows an increase of α by the same factor. Therefore, the transmission is increased by g^2.

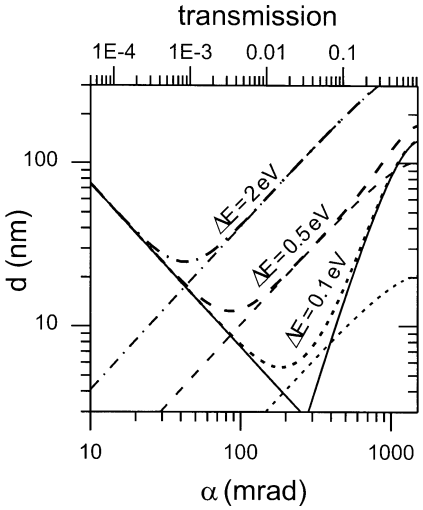

Fig. 2. Influence of the energy spread ΔE on the resolution limit dependence $d(\alpha)$ at a start energy $E_0 = 1$ eV. Thick dotted, dashed and dash–dotted lines correspond to $\Delta E = 0.1$ eV, 0.5 eV and 2 eV. The thin solid lines are the contributions from the diffraction limit and the spherical aberrations.

Taking into account that reducing the energy slit by a factor of g lowers the image intensity by g, the net gain of intensity is g.

3.2. *Corrected systems*

A tetrode mirror as suggested by D. Preikszas and H. Rose[10] compensates simultaneously for the spherical and the chromatic aberration. The accompanying special beam splitter is corrected in second order and does not introduce dispersion up to second degree. The OMEGA filter is also corrected to second order. As a consequence, the remaining aberrations of the whole system are of higher rank:

$$d_s^{(5)} = C_{ss}\sin^5\alpha\,, \tag{5}$$

$$d_c^{(3)} = C_{cc}\left(\frac{\Delta E}{E}\right)^2\sin\alpha\,, \tag{6}$$

$$d_{sc}^{(4)} = C_{sc}\frac{\Delta E}{E}\sin^3\alpha\,. \tag{7}$$

Here the superscript indicates the rank of the aberration.

The theoretical resolution limit of the SMART with and without corrector is depicted in Fig. 3. A start energy $E_0 = 10$ eV, an energy spread $\Delta E = 2$ eV, and an acceleration field of 5 kV/mm in front

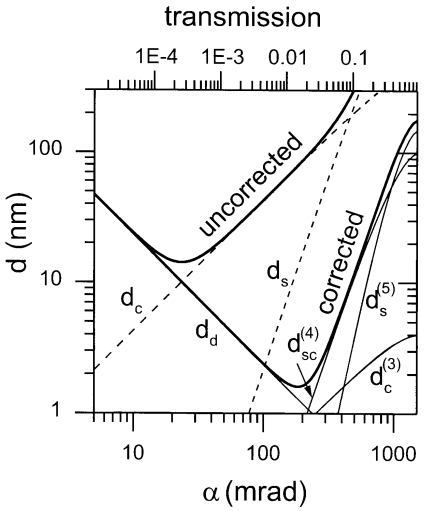

Fig. 3. Resolution limit d as a function of the acceptance angle α for the corrected and uncorrected SMART in the cases $E_0 = 10$ eV and $\Delta E = 2$ eV. The dominating aberration components are added; dashed lines for the uncorrected and thin solid lines for the corrected case.

of the sample are assumed. The dominating aberration contributions are given for the uncorrected and the corrected case. The corrector reduces the resolution limit of the uncorrected system from 14 nm to 1.6 nm. In parallel, the transmission increases by a factor of 67. Alternatively, if the corrected system operates with a resolution limit of 14 nm, the gain in transmission increases to 500 compared with that of the uncorrected system. Both the increase in resolution and in transmission will be the outstanding features of the aberration-corrected version of the SMART microscope.

The faster the electrons start from the sample surface, the smaller are the resolution limit d and the transmission T, as shown in detail in Fig. 4. The reduction of the energy spread ΔE by the analyzer improves both the resolution and the transmission, especially at low start energies. For the uncorrected system this gain in transmission nearly compensates for the loss in image intensity caused by the reduced energy slit width (see Subsec. 3.1). The corrector drastically improves resolution and transmission. A simultaneous gain between 3 and 7 in resolution and between 10 and 50 in transmission (compare open and full symbols in Fig. 4) is achieved. Only at low start energies (below $E_0 = 5$ eV) and wide energy spreads ($\Delta E > 3$ eV) does the corrector

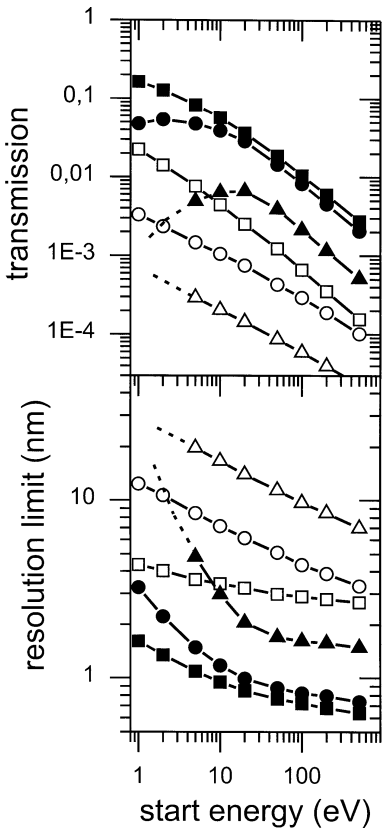

Fig. 4. Resolution limit and transmission with (full symbols) and without (open symbols) aberration correction as a function of the start energy E_0 at different energy spreads $\Delta E = 0.1$ eV (squares), 1 eV (circles) and 5 eV (triangles) for optimized aperture sizes. Data from Ref. 22.

not appreciably improve resolution and transmission. This situation is given for secondary photoelectron emission microscopy using synchrotron light (XPEEM) without energy filtering. In such XPEEMs the corrector will not be able to significantly improve the performance of the instrument, but is only useful in combination with an energy filter which reduces the energy spread ΔE.

4. Experimental Results

A spectroscopic PEEM (a PEEM equipped with an imaging analyzer for energy filtering) enables three modes of operation:[6]

(i) Microscopy;
(ii) Spectroscopy;
(iii) Angular distribution measurements.

Microscopy is performed with (a) a fixed acceptance angle obtained by an aperture, (b) usually in normal emission, (c) at a chosen kinetic electron energy E_0 (start energy), and (d) at fixed energy window ΔE set by the energy slit. *Spectroscopy* can be done in two modes: (A) The dispersion plane of the analyzer is directly imaged at fixed angular acceptance (using the angle-limiting aperture) and with a chosen "surface area of interest" by using the field-limiting aperture; (B) the (so-called) indirect spectroscopy is based on the accumulation of microscopic images taken with different (i.e. scanned) electron or photon energies. The subsequent numerical analysis of the digital data selects distinct surface areas of interest — leading to the so-called "stack analysis."

The same procedure can be done for stacks of *images of the angular distributions*. The imaging of the angular distribution in the spectroscopic PEEM corresponds — from the optical point of view — to the LEED mode in a LEEM instrument. In this mode the angular distribution of the emitted electrons is directly imaged onto the detector at a chosen start energy E_0 with a selected energy window ΔE (analyzer slit) and with a chosen "surface area of interest" by using the field aperture.

Examples for these modes measured with the current version of the SMART will be given in the following sections.

4.1. *Microscopy*

As a test system we used three-dimensional graphite islands on a Ag(111) single crystal which were obtained by photolytic decomposition of NTCDA crystallites. Figure 5 shows on the left an image of this surface at a moderate magnification of 2200 with secondary electrons at $E_0 = 0.9$ eV. The image on the right hand side was taken with the Ag 3d photoemitted electrons at $E_0 = 71.2$ eV. The energy window of the filter was set to $\Delta E = 0.5$ eV; the photon energy was $h\nu = 450$ eV with an energy resolution of $\Delta E_{\mathrm{ph}} = 0.1$ eV.

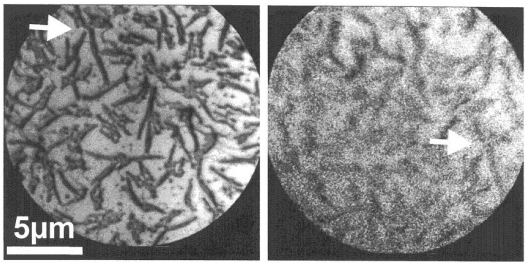

Fig. 5. Energy-filtered microscopy. Image of graphite islands on Ag(111) taken with secondary electrons at $E_0 = 0.9$ eV (*left*) and with the Ag $3d_{3/2}$ photoemitted electrons at $E_0 = 71.2$ eV (*right*). The arrows mark the same surface spot.

The secondary electron image reveals a strong contrast due to the different yield of secondary emitted electrons from the Ag substrate and the graphite islands. Of course, an unambiguous assignment of light and dark areas to substrate and graphite in such a single image is only possible if the relative yield of the secondary processes is known for graphite and Ag at that specific energy or by tuning the photon energy to the resonant emission of carbon (NEXAFS). In our case we tuned the electron energy to the photoemission peak of Ag $3d_{3/2}$ (Fig. 5, right). Under this condition the image intensity can be analyzed qualitatively: the bright areas are due to the Ag substrate, the dark areas to the graphite islands. Though the surface is shifted in the observed field of view, identical surface spots can be identified, as indicated by the arrows. Unfortunately, the quality of the Ag 3d-photoemitted electron image is poor due to a misalignment of the objective lens and low intensity which could not be optimized because of a lack of the time.

Extensive experiments to improve and demonstrate the lateral resolution of the present setup have not yet been performed since presently the here used objective lens is being reconstructed. However, in previous laboratory experiments a lateral resolution of 50 nm was achieved, which — under the available conditions at that time — was considered to be a good starting point.

4.2. *Spectroscopy*

For a comprehensive analysis of chemical states and compounds, the spectroscopic mode is the best choice. Figure 6 shows the Ag 3d doublet and the C 1s peak, both taken with 450 eV photon energy using a photon energy resolution of $\Delta E_{\mathrm{ph}} = 0.1$ eV. The top row shows the dispersion plane imaged on the detector with horizontal energy axis. The specimen potentials for the Ag and the C peaks were set to 70.5 V and 158 V, respectively, in order to position the energy ranges to be studied on the detector. The

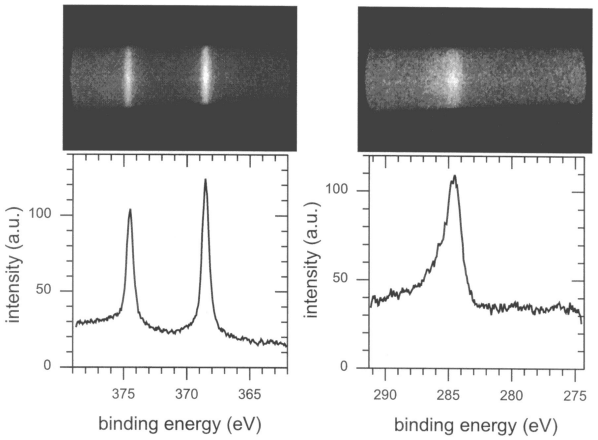

Fig. 6. Spectroscopy mode: imaging of the dispersion plane of the analyzer. Left — Ag 3d doublet; right — C 1s; top row — raw data on the detector screen; bottom row — the integrated intensity. The photon energy was $h\nu = 450$ eV.

detected energy range at this specific measurement amounts to 17 eV, but can be increased to a maximum of 30 eV, mainly by changing the settings of the projector optics. The spectra shown in the lower part of Fig. 6 are generated simply by numerical integration of the raw data. In order to enhance the dynamical range of the detector system by up to two orders of magnitude, the energy focus is stretched perpendicular to the energy axis by a specific quadrupole in the OMEGA filter. This procedure results in quite smooth spectra which are taken with a simple eight-bit camera.

For these spectra an object area with a diameter of 3 μm was selected by the field aperture. The magnification of the transfer optics of the SMART in principle allows sizes of selected areas down to less than 10 nm. The measured full width at half maximum of the Ag 3d peaks is 0.65 eV. A deconvolution gives an overall spectral resolution of less than 0.5 eV, which for first test measurements is a reasonably good value for this kind of microscope.

4.3. *Angular distribution measurements*

The third mode of operation to be demonstrated in the SMART instrument concerns the imaging of the angular distribution of the emitted electrons. A special setting of the electron optics exchanges the image of the object plane with that of the back focal plane in which the angular distribution is available. As a consequence, the intermediate image of the surface is formed in the plane of the aperture which previously limited the acceptance angle. Now this aperture acts as a field aperture enabling the selection of an area of interest down to 250 nm in diameter.

Figure 7 shows the angular distribution of the secondary electrons for different kinetic energies in the range between 11 eV and 21 eV taken with an

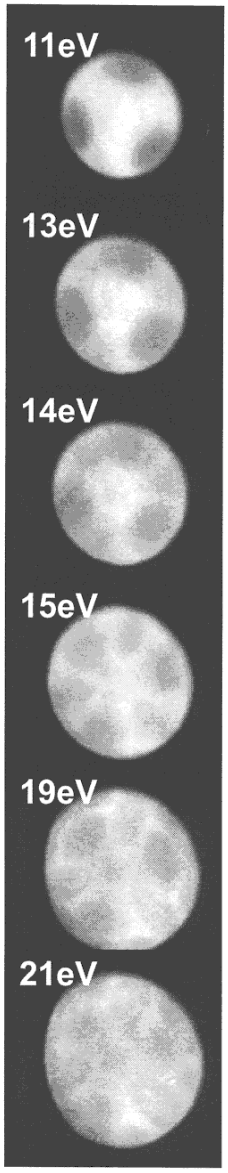

Fig. 7. Imaging of the angular distribution of the secondary electrons at a photon energy $h\nu = 450$ eV. The kinetic energy of the electrons is varied from 11 eV to 21 eV.

energy window $\Delta E = 0.5$ eV set by the OMEGA filter. The size of the object area selected by the aperture is 1 μm in diameter in all cases. Due to the strong acceleration of the electrons from the initial energy to the base energy of 15 keV, the instrument is able to utilize the full angular half sphere (2π). Thus the center of each image in Fig. 7 corresponds to normal emission and the outer edge to the $\pm 90°$ emission. In other words, the electrons at the edge start parallel to the surface. As expected for this kind of microscope, the diameter of the disklike image of the angular distribution grows with the square root of the initial kinetic energy. This is well known from the LEED pattern in LEEM instruments, where the disk represents the Ewald sphere. Using the known LEED spot position, a calibration of the momentum $\mathbf{k}_{\|}$ parallel to the surface is easily possible. The momentum calibration is the same for all kinetic energies. As a consequence the LEED spot positions remain at the same place on the detector while the kinetic energy is changed.

The origin of the pronounced threefold pattern of the secondary emission is a combination of the electron energy dispersion $E(\mathbf{k})$ (i.e. the band structure) and of diffraction processes of the emitted electrons (i.e. photoelectron diffraction). A quantitative analysis is, of course, complicated — and hence has not been tried for the present preliminary data — because band structure calculations and calculations of the final state wave function and its coupling to the emitted wave have to be performed. However, only for a qualitative characterization of the crystal symmetry is this method very helpful: the threefold symmetry of the Ag(111) crystal is clearly visible.

The photoelectron diffraction pattern of the Ag 3d doublet shown in Fig. 8 allows, in principle, a quantitative analysis of the local atomic geometry of the Ag emitter. Thus images were taken at three different photon energies; at each photon energy the kinetic energies were tuned to the Ag $3d_{3/2}$ and the Ag $3d_{5/2}$ peaks (left and right column, respectively). The energy window was set to $\Delta E = 0.5$ eV. The outstanding performance of this mode is demonstrated by an acquisition time of only 60 s, sufficient even for a selected area of interest of only 1 μm in diameter. This behavior results from the parallel detection method, which requires considerably less time than the usual mechanical scanning method. The angular detection range in this mode is, in principle, again $\pm 90°$. The border in Fig. 8, however, is limited by the aperture placed in the diffraction plane.

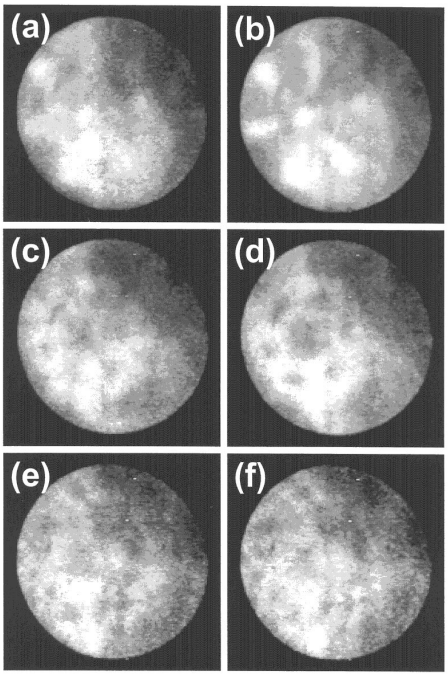

Fig. 8. Photoelectron diffraction: imaging of the angular distribution of the Ag $3d_{3/2}$ (left column) and Ag $3d_{5/2}$ emitted electrons at different photon energies $h\nu = 430$ eV (a), (b), $h\nu = 450$ eV (c), (d) and $h\nu = 470$ eV (e), (f), corresponding to kinetic energies of 50.8/56.8 eV, 70.8/76.8 eV and 90.8/96.8 eV (a)–(f).

5. Conclusions

This paper first considers the most important parameters of imaging, corrected or uncorrected spectromicroscopes, namely lateral resolution and transmission. Secondly, the present status of the SMART project is briefly reviewed, and first results are presented using the second development stage of the SMART instrument, an already energy-filtered but yet uncorrected PEEM version. Theoretical calculations show that at low start energies below 10 eV energy filters significantly reduce chromatic aberration and therefore improve resolution and transmission. Most existing PEEM instruments have not yet reached their theoretical resolution limit of about 10 nm. Besides some instrumental problems like mechanical vibrations or instabilities of the power supplies, the lack of image intensity is the

largest obstacle to improving the resolution. Either the aperture is chosen too large in order to enable high transmission or, at optimal aperture size, a low image intensity forces such long acquisition times that (a) the (re)alignment of the optics setting can hardly be done in an acceptable time, and (b) the system is very sensitive to instabilities. These effects demonstrate the fundamental necessity to increase the transmission by both energy filtering and aberration correction.

For our example of graphite islands on Ag(111) we could show that a PEEM with imaging analyzer enables imaging with electrons not only at secondary emission, but also at higher energies. This allows one to utilize any of the three operation modes: microscopy (including imaging with electrons of a selected photoemission peak), photoelectron spectroscopy, and angular distribution measurements (including photoelectron diffraction). These different methods allow a comprehensive characterization of surfaces.

The performance of the second development step of the SMART spectromicroscope could be shown, and some remarkable features could be demonstrated. The microspectroscopy mode with its parallel detection of a spectral range up to 30 eV wide can be done on selected areas down to a few tens of nanometers in size with an energy resolution of better than 0.5 eV (demonstrated was already 1 μm). This mode enables a very fast chemical characterization of the surface, which can be investigated in detail in the microscopy mode at some characteristic energies. The micro-photoelectron diffraction (μ-PED) mode allows the probing of objects even on a submicrometer scale. As a consequence, PED is possible not only on homogeneous large single crystals but also on single microcrystals in polycrystalline samples, individual islands, single superstructure domains, reaction fronts, etc.

The next goal is the combination of the corrector with the present energy-filtering PEEM. As a first result, which can easily be achieved, the transmission will be drastically increased by a factor of 30–50, if one accepts the same lateral resolution as in the uncorrected system. In a second step, after optimizing the alignment and the mechanical and electrical stability of the instrument, the resolution will be improved. The final aim will be a lateral resolution of at least 2 nm in the LEEM and 5 nm in the PEEM mode.

Acknowledgments

This project is funded by the Federal German Ministry of Education and Research (BMBF) under contracts No. 05 644 WWA9 and 05 SL8 WW8-1. We gratefully acknowledge support by the BESSY crew, especially Drs. C. Jung and R. Follath. One of us (E. U.) wishes to thank the Fond der Chemischen Industrie for financial support.

References

1. Th. Schmidt and E. Bauer, *Phys. Rev.* **B62**, 15815 (2000); Th. Schmidt and E. Bauer, *Surf. Sci.* **480**, 137 (2001).
2. F.-J. Meyer zu Heringdorf, R. Hild, P. Zahl, Th. Schmidt, B. Ressel, S. Heun, E. Bauer and M. Horn-von Hoegen, *Surf. Sci.* **480**, 103 (2001); F.-J. Meyer zu Heringdorf, Th. Schmidt, S. Heun, R. Hild, P. Zahl, B. Ressel, E. Bauer and M. Horn-von Hoegen, *Phys. Rev. Lett.* **86**, 5088 (2001).
3. Th. Schmidt, A. Schaak, S. Günther, B. Ressel, E. Bauer and R. Imbihl, *Chem. Rev. Lett.* **318**, 549 (2000).
4. Spectromicroscopy issue of *J. Electron Spectrosc. Relat. Phenom.*, ed. H. Ade **84** (1997).
5. R. M. Tromp, M. Mankos, M. C. Reuter, A. W. Ellis and M. Copel, *Surf. Rev. Lett.* **5**, 1189 (1998).
6. Th. Schmidt, S. Heun, J. Slezak, J. Diaz, K. C. Prince, G. Lilienkamp and E. Bauer, *Surf. Rev. Lett.* **5**, 1287 (1998).
7. S. Anders, H. A. Padmore, R. M. Duarte, T. Renner, T. Stammler, A. Scholl, M. R. Scheinfein, J. Stöhr, L. Seve and B. Sinkovic, *Rev. Sci. Instrum.* **70**, 3973 (1999).
8. O. Scherzer, *Optik* **2**, 114 (1936).
9. R. Fink, M. R. Weiß, E. Umbach, D. Preikszas, H. Rose, R. Spehr, P. Hartel, W. Engel, R. Degenhardt, H. Kuhlenbeck, R. Wichtendahl, W. Erlebach, K. Ihmann, R. Schlögl, H.-J. Freund, A. M. Bradshaw, G. Lilienkamp, Th. Schmidt, E. Bauer and G. Benner, *J. Electr. Spectrosc. Relat. Phenom.* **84**, 231 (1997).
10. D. Preikszas and H. Rose, *J. Electr. Micr.* **1**, 1 (1997).
11. H. Müller, D. Preikszas and H. Rose, *J. Electr. Micr.* **48**, 191 (1999).
12. P. Hartel, Dissertation D17, Technische Hochschule Darmstadt, Germany (2001).
13. H. Rose and D. Krahl, in *Energy-Filtering Transmission Electron Microscopy* (Springer, Berlin, 1995), ed. L. Reimer, p. 43.
14. M. Merkel, M. Escher, J. Settemeyer, D. Funnemann, A. Oelsner, Ch. Ziethen, O. Schmidt, M. Klais and G. Schönhense, *Surf. Sci.* **480**, 196 (2001).
15. C. Quitmann, U. Flechsig, L. Patthey, T. Schmidt, G. Ingold, M. Howells, M. Janousch and R. Abela, *Surf. Sci.* **480**, 173 (2001).

16. J. Feng, private communication.
17. V. Kolařík, R. Vašina, M. Mynář and T. Bejdák, in *Proc. 12th European Congress on Electron Microscopy*, Vol. III (CSEM, Brno, Czech Republic, 2000), eds. P. Tománek and R. Kolařík, p. I 181.
18. R. Wichtendahl, R. Fink, H. Kuhlenbeck, D. Preikszas, H. Rose, R. Spehr, P. Hartel, W. Engel, R. Schlögl, H.-J. Freund, A.M. Bradshaw, G. Lilienkamp, Th. Schmidt, E. Bauer, G. Benner and E. Umbach, *Surf. Rev. Lett.* **5**, 1249 (1998).
19. L. H. Veneklasen, *Rev. Sci. Instrum.* **64**, 5513 (1992).
20. E. Bauer, T. Franz, C. Koziol, G. Lilienkamp and Th. Schmidt, in *Chemical, Structural and Electronic Analysis of Heterogeneous Surfaces on Nanometer Scale* (Kluwer, Dordrecht, 1997), ed. R. Rosei, p. 75.
21. C. Jung, J. Bahrdt, U. Flechsig and M. R. Weiß, in *Proc SPIE*, Vol. 3150 (San Diego, 1997), p. 148.
22. D. Preikszas, Dissertation D17, Technische Hochschule, Darmstadt, Germany (1995).
23. E. Bauer, *Ultramicroscopy* **36**, 52 (1991).